

A Model For Polarised Microwave Foreground Emission From Interstellar Dust

D. T. O’Dea¹, C. N. Clark^{1*}, C. R. Contaldi¹ and C. J. MacTavish²

¹*Theoretical Physics, Blackett Laboratory, Imperial College, London, UK*

²*Kavli Institute for Cosmology, University of Cambridge, Cambridge, UK*

25 December 2021

ABSTRACT

The upcoming generation of cosmic microwave background (CMB) experiments face a major challenge in detecting the weak cosmic B -mode signature predicted as a product of primordial gravitational waves. To achieve the required sensitivity these experiments must have impressive control of systematic effects and detailed understanding of the foreground emission that will influence the signal. In this paper, we present templates of the intensity and polarisation of emission from one of the main Galactic foregrounds, interstellar dust. These are produced using a model which includes a 3D description of the Galactic magnetic field, examining both large and small scales. We also include in the model the details of the dust density, grain alignment and the intrinsic polarisation of the emission from an individual grain. We present here Stokes parameter template maps at 150 GHz and provide an on-line repository[†] for these and additional maps at frequencies that will be targeted by upcoming experiments such as EBEX, SPIDER and SPTpol.

Key words: cosmic microwave background, polarisation experiments, foregrounds, B -modes, gravity waves

1 INTRODUCTION

The next round of cosmic microwave background (CMB) experiments are all targeting measurements of CMB polarisation. The CMB polarisation field can be decomposed into curl-free E -modes and curl-like B -modes (see for example Kamionkowski, Kosowsky & Stebbins (1997)), however to date only E -modes have been observed (Kovac et al. 2002; Readhead et al. 2004; Sievers et al. 2007; Barkats et al. 2005; Bischoff et al. 2008; Leitch et al. 2005; Montroy et al. 2006; Piacentini et al. 2006; Wu et al. 2007; Page et al. 2007; Brown et al. 2009; Chiang et al. 2010; QUIET Collaboration 2010). Current work centres on the search for the tiny amplitude B -modes since a key prediction of inflation is the generation of a stochastic background of gravitational waves, which on large angular scales are the only contribution to the CMB B -mode component. Experiments involved in this search include EBEX (Reichborn-Kjennerud et al. 2010), SPIDER (Filippini et al. 2010), SPTpol (McMahon et al. 2009), PIPER (Lazear et al. 2011), ABS (Essinger-Hileman et al. 2010), ACTpol (Niemack et al. 2010), POLAR (Keating et al. 1998), POLARBEAR (The Polarbear Collaboration et al. 2010) and BRAIN (Charlassier & the BRAIN Collaboration 2008). We focus on providing templates at

frequencies being targeted by EBEX, SPIDER and SPTpol. Galactic foreground emission is expected to contribute significantly to the polarised microwave emission across the sky, and may well dominate the CMB gravitational-wave signal at all frequencies. In order to achieve their scientific goals, forthcoming CMB polarisation experiments require in-depth knowledge of this polarised Galactic foreground emission. The PLANCK mission (The Planck Collaboration 2006) will provide maps of the polarisation of interstellar dust, allowing tests of the structure of the Galactic magnetic field. It should also provide an insight into grain alignment mechanisms.

Of utmost importance will be the accurate separation of foreground emission from the CMB signal. Component separation has been considered in, for example, Brandt et al. (1994); Eriksen et al. (2006); Kogut et al. (2007); Stompor et al. (2009). In order to test and assess methods for separating out the contribution realistic foreground templates will be required. Since however, few data exist at this time at the observing frequencies in which the upcoming experiments are operating, one must resort to modeling of foreground emission by extrapolating the information from existing data. Furthermore, experiments which observe portions of the sky close to the Galactic plane will find the foreground emission is very bright in comparison to the CMB. The presence of this bright emission in the data may affect

* E-mail: caroline.clark05@imperial.ac.uk

the performance of the observation and the analysis strategy an experiment uses. Another important role of foreground modeling, therefore, is informing the planning and proposal stage of any experiment.

Unfortunately, these foregrounds are poorly constrained by current data and poorly understood, particularly above around 90 GHz, where the CMB emission is strongest and where many new CMB experiments will operate. At these frequencies, the foreground emission is expected to be dominated by thermal emission from interstellar dust. A review of the basic physical processes whereby aligned dust grains generate polarisation is given in Lazarian & Cho (2003). Such emission is known to be polarised both through direct measurements (Ponthieu et al. 2005; Kogut et al. 2007; Benoît et al. 2004; Bierman et al. 2011) and through observations of the polarisation of starlight (Heiles 1996; Fosalba et al. 2002).

This polarisation arises due to the presence of a magnetic field in the Galaxy. The dust grains are generally non-spherical, and preferentially emit radiation polarised along their longest axis. Mechanisms exist which align these grains with this axis perpendicular to the Galactic magnetic field, leading to net linear polarisation.

Polarised foregrounds also include polarised emission from synchrotron. Synchrotron emission, generated by the gyration of cosmic ray electrons in the Galactic magnetic field, is intrinsically polarised and constitutes the main polarised foreground at lower frequencies (Page et al. 2007). However, emission from thermal dust dominates synchrotron emission at the frequencies considered in this paper and therefore we concentrate on modeling emission from only thermal dust. Foreground radiation also includes free-free and spinning dust emission, however we assume both of these signals to be unpolarised and so do not consider them further here. Evidence for this has emerged recently, with Macellari et al. (2011) showing that free-free emission is unpolarised, setting an upper limit on the free-free polarisation fraction of 3.4% at the 2σ level. They also show that spinning dust emission has a low polarisation fraction. Upper limits on the polarisation fraction of spinning dust emission in molecular clouds have been obtained by Dickinson, Peel & Vidal (2011) and López-Caraballo et al. (2011), who find low levels of polarisation. If there is a similar level at higher Galactic latitude, then this foreground is unimportant in terms of component separation.

The model in this paper was introduced by O’Dea (2009) and first applied in O’Dea et al. (2011) for the purpose of studying the impact of polarised foregrounds on Spider’s ability to detect B -mode polarisation. Here we give a more detailed explanation of the model and present a number of full-sky template maps at various frequencies. ARCHEOPS (Benoît et al. 2004) and BICEP (Bierman et al. 2011) have made the highest signal-to-noise maps of the dust polarisation at low Galactic latitudes and have examined the properties of the polarisation fraction and angle. These results cannot be relied upon to calibrate large scale models of the polarisation at higher latitudes since the polarisation properties near the Galactic plane will depend on complex structure that is not included in models such as the one presented in this work. Here, both polarisation amplitude and angle are modeled internally and our templates are scaled such that the polarisation fraction corresponds

to a nominal value when averaged over the maps with the Galaxy masked out. The ARCHEOPS and BICEP maps have not been made public and a quantitative comparison of our templates with these observations is not possible. Fauvet, L. et al. (2011) have developed a similar model of both the polarisation of thermal dust and synchrotron radiation and compared with the WMAP K-band and ARCHEOPS 353GHz data, however they have not released any templates based on their model.

This paper is organized as follows. We begin in Section 2.1 by describing the model of the dust total intensity. We focus on modeling the Galactic magnetic field (which is made up of a large-scale field from the Galactic disk and a small-scale field due to turbulence in the interstellar plasma) in Section 2.2. We include in Section 2.3 a description of the large-scale dust density, as well as details of the treatment of dust grain alignment and the intrinsic polarisation of the emission from an individual grain. In Section 2.4 we show how these fields are modeled in three-dimensions and are used to perform a line-of-sight integral to the centre of each pixel to form the final Stokes parameter maps. In Section 3 we discuss the effective resolution of the maps produced using our model and the relevant physical scales introduced by various effects. In Section 4 we describe the final template maps and summarise our conclusions in Section 5.

2 FOREGROUND DUST MODEL

2.1 Dust Total Intensity

Although few data are available regarding the polarised emission from dust, the same is not true of its total intensity. In particular, the IRAS satellite observed this emission across the sky at $100\mu\text{m}$ and $240\mu\text{m}$, close to the peak in the dust emission. By constraining physically-motivated extrapolations of these observations using further data, Finkbeiner, Davis & Schlegel (1999, hereafter FDS) provided models of the emission at microwave wavelengths. At 94 GHz, these models have been shown to agree well in terms of morphology with the WMAP observations with some minor structural differences on the Galactic Plane (Gold et al. 2009). However, there are indications that in terms of amplitude the WMAP dust template fit coefficients differ by about 30%. Bennett et al. (2003) suggest that this is possibly due to the degeneracy that exists between the strongly correlated dust and synchrotron emission components in the simultaneous fit of their externally derived template maps to WMAP data.

In the higher frequency bands relevant to experiments observing above ~ 90 GHz, data are more limited but agree well with the FDS predictions (Culverhouse et al. 2010; Veneziani et al. 2010). We will use this model (to be precise model number eight in FDS) to trace the total intensity of the dust emission. We exploit the full, 6.1 arcminutes, resolution of the IRAS data by pixelising the dust intensity on HEALPIX (Górski et al. 2005) maps of $N_{\text{side}}=1024$.

2.2 Galactic Magnetic Field

The degree and direction of polarisation of the dust emission are highly dependent on the Galactic magnetic field. As

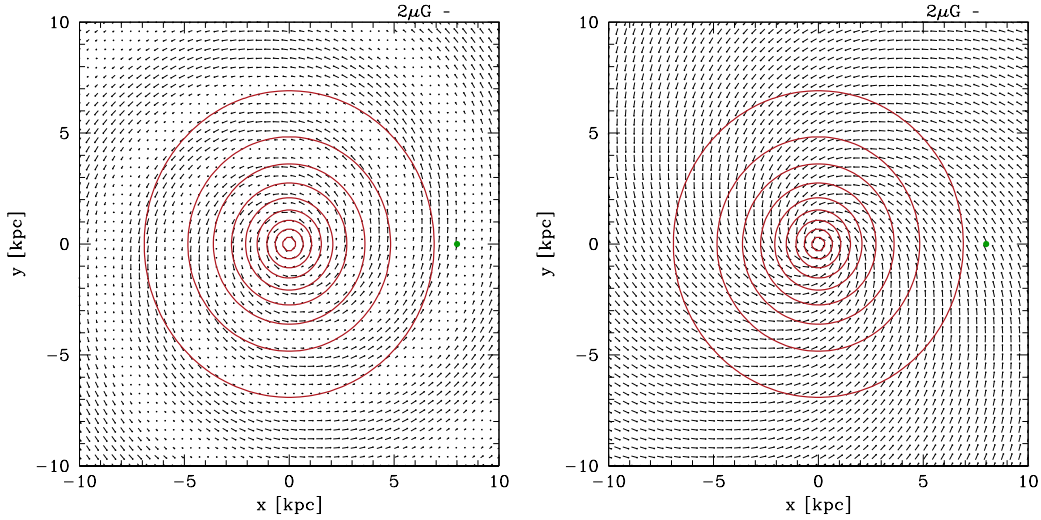


Figure 1. Cartesian projection of the BSS (left panel) and LSA (right panel) large-scale magnetic field models, showing a slice through the Galactic plane observed along the positive z -axis. The filled circle represents the position of the Sun in relation to the Galactic centre. The alignment and magnitude of the magnetic field are shown as headed ticks with the $B_0 = 2 \mu\text{G}$ scale represented at the top of each panel. The red solid lines are the density contours, in steps of 0.1, of the dust density model $n_d(r, z)$ (see Section 2.3) used in the line-of-sight integration. The dust density is normalised to 1 at the Galactic centre.

the observed polarisation is the sum of many independent regions along the line-of-sight, it is sensitive to the three-dimensional structure of this magnetic field. Therefore, to proceed we first consider a three-dimensional model of the Galactic magnetic field (and the other necessary Galactic constituents and physics) and then set the polarisation degree and direction through the appropriate line-of-sight integrals.

Away from the Galactic center, the Galactic magnetic field is usually considered to have two near-independent components: a large-scale coherent field associated with the Galactic disk, and a small-scale field arising from turbulence in the interstellar plasma sourced by astrophysical events such as supernovae and stellar winds. The most informative probes of these fields are Faraday rotation measures of pulsars and extra-Galactic radio sources (Haverkorn et al. 2006; Han et al. 2006). Whilst there is general agreement that the large-scale field follows a spiral pattern, its detailed structure is still uncertain.

When considering areas of sky at high Galactic latitudes, this uncertainty is unimportant as the dust is concentrated in a thin disk about the Galactic plane, and so we only see emission within around 1 kpc or so of the Sun, a region in which the large-scale field is reasonably well characterised. However, experiments which will target a large fraction of the sky, possibly including part of the Galactic plane, will require a model of the large-scale field structure in the plane.

Attempts have been made to constrain the properties of the magnetic field using CMB polarisation measurements. Jaffe et al. (2010) use an Monte Carlo Markov Chain (MCMC) approach to test components of a 2D Galactic field model using rotation measures and WMAP data in the plane of the Galaxy. Jansson et al. (2009) use rotation measures and WMAP 5 year data to fit for parameters in common 3D models for the Galactic magnetic field. We choose

two of the most popular forms for the Galactic magnetic field and provide templates for both of these models.

2.2.1 Large-Scale Magnetic Field

One popular candidate is the Bi-Symmetric Spiral (BSS) (Han & Qiao 1994; Sun et al. 2008) which can be written as

$$\begin{aligned} B_\rho &= -B_0 \cos \left(\Phi + \psi \ln \frac{\rho}{\rho_0} \right) \sin p \cos \chi, \\ B_\Phi &= -B_0 \cos \left(\Phi + \psi \ln \frac{\rho}{\rho_0} \right) \cos p \cos \chi, \\ B_z &= B_0 \sin \chi. \end{aligned} \quad (1)$$

Here, ρ , Φ and z are Galacto-centric cylindrical co-ordinates with Φ , the cylindrical longitude, measured from the direction of the Sun, p is the pitch angle of the field, $\psi = 1/\tan p$, ρ_0 defines the radial scale of the spiral, $\chi = \chi_0 \tanh(z/z_0)$ parametrizes the amplitude of the z component and $z_0 = 1$ kpc. We use the parameters constrained in Miville-Deschênes et al. (2008): $p = -8.5$ degrees, $\rho_0 = 11$ kpc and $\chi_0 = 8$ degrees, with the field amplitude set to $B_0 = 3 \mu\text{G}$, and take the distance between the Sun and the Galactic center to be 8 kpc. A diagram of the magnetic field orientation and magnitude in the BSS model is shown in the left panel of Figure 1.

A number of other magnetic field models have been proposed in the literature. For comparison we also include the Logarithmic Spiral Arm (LSA) model introduced by Page et al. (2007) for use in cleaning of the WMAP data. The

model is defined as

$$\begin{aligned} B_\rho &= -B_0 \sin\left(\psi_0 + \psi_1 \ln \frac{\rho}{\rho_W}\right) \cos \chi, \\ B_\Phi &= -B_0 \cos\left(\psi_0 + \psi_1 \ln \frac{\rho}{\rho_W}\right) \cos \chi, \\ B_z &= B_0 \sin \chi, \end{aligned} \quad (2)$$

with parameters obtained by fits to the WMAP K-band field directions; $\psi_0 = 27$ degrees, $\psi_1 = 0.9$ degrees, and χ defined as in the BSS model but with $\chi_0 = 25$ degrees. The radial scale is also different in this model with $\rho_W = 8$ kpc whereas the scale height is the same as above with $z_0 = 1$ kpc. There is no azimuthal dependence in this model. The right panel of Figure 1 shows a slice through the Galactic plane for the LSA model.

Although both fields are unlikely to provide a full description of our Galaxy (Men, Ferrière & Han 2008; Sun et al. 2008), they are sufficient for our current purpose as we do not require a precise template of the sky, only a reasonable approximation against which to test foreground separation techniques and the performance of experiments in the presence of systematic effects.

Both magnetic field models assume the field strength B_0 is constant although there is weak evidence for some radial dependence (Han et al. 2006). Any such dependence will not affect the polarisation model significantly and the overall radial dependence of the signal is determined by the exponential drop-off in the dust density which modulates the integrand along the line-of-sight. Field reversals may also be present in the spiral arms but, if sharp enough, will not contribute to the signal significantly.

2.2.2 Small-Scale Galactic Magnetic Field

The turbulent field is somewhat less well understood. When constraining the above large-scale field, Miville-Deschênes et al. (2008) simultaneously fit a small-scale field with best-fit r.m.s amplitude $B_{\text{r.m.s.}} = 1.7 \mu\text{G}$. Several different studies agree that the r.m.s. amplitude is similar to the amplitude of the large-scale field in the Solar vicinity (Fosalba et al. 2002; Han et al. 2006), and so here we set $B_{\text{r.m.s.}} = 2 \mu\text{G}$. Minter & Spangler (1996) examined the rotation measures of extra-Galactic sources across a small patch of sky and concluded that the data were consistent with Kolmogorov turbulence on scales smaller than 4 pc, assuming a statistically isotropic, homogeneous Gaussian field. On larger scales they found a somewhat flatter energy spectrum with an outer scale of up to 96 pc. Kolmogorov-type spectra up to kilo-parsec scales in the interstellar magnetic field and other interstellar plasma components have also been reported by other studies (Armstrong, Rickett & Spangler 1995; Lazarian & Pogosyan 2000; Cho & Lazarian 2008).

Kolmogorov turbulence describes the energy distribution among vortices of different size, with the amplitude of the turbulence related to the energy density at that position. Turbulent flow can be viewed as an energy cascade from larger to smaller eddies. At small enough length scales, known as the Kolmogorov length scale, energy is dissipated through viscous dissipation. A Kolmogorov spectrum is proportional to the rate of energy dissipation and the magnitude of the wavevector k . Using the Kolmogorov energy

spectrum one finds that the power spectrum of a turbulent field is $\mathcal{P}(k) \propto k^{-(2+3N_d)/3}$ where N_d is the number of spatial dimensions of the realisation. In this work, we generate realisations of this power spectrum in order to model the three-dimensional magnetic field in real space by a Fast Fourier Transform (FFT).

It is numerically intractable to generate a realisation of this turbulent field in three dimensions at sufficiently high resolution and to accommodate the entire sky, hence we resort to independent one-dimensional realisations along the line-of-sight to each pixel. This model ignores correlations across the sky, but properly incorporates the line-of-sight depolarisation. We choose an injection scale of 100 pc, assume the dissipation scale is small and use the one-dimensional Kolmogorov energy spectral index of $-5/3$.

For smaller patches of the sky, relevant for ground-based observations, a full, three dimensional realisation is feasible together with a higher angular resolution in the line-of-sight integrals.

2.3 Dust Properties

We model the large-scale spatial distribution of the dust density, n_d , using a simplification of the model constrained in Drimmel & Spergel (2001),

$$n_d = n_0 \exp\left(-\frac{\rho}{\rho_d}\right) \text{sech}^2\left(\frac{z}{z_d}\right). \quad (3)$$

For consistency with the WMAP polarisation analysis (Page et al. 2007), we take the scale height $z_d = 200$ pc and the scale radius $\rho_d = 3$ kpc. We do not attempt to model the small-scale variations in the dust density and temperature here, which may also affect the polarisation degree and direction. Small-scale variations in the total intensity are included via the FDS model.

The model also requires a description of the physics of grain alignment and of the intrinsic polarisation of the emission from an individual grain. In general these are complex functions of the magnetic field and various properties of the grains. Recently, good progress has been made in describing the details of the alignment using the theory of radiative torques (Lazarian & Hoang 2007; Hoang & Lazarian 2008). However, it is still difficult to produce a well-constrained quantitative description to apply to our model (Lazarian & Hoang 2009).

Instead, we describe the alignment in an integrated manner, without recourse to the details of a particular physical mechanism. We assume that the polarisation direction is always perpendicular to the component of the magnetic field in the plane of the sky, and that the degree of polarisation depends quadratically on the magnetic field strength. This is similar to the behaviour assumed in Page et al. (2007). We follow this approach in providing our templates and do not attempt to account for any possible misalignment of the axis of orientation of the dust grains with the magnetic field lines, as is done in other work, for example Fauvet, L. et al. (2011).

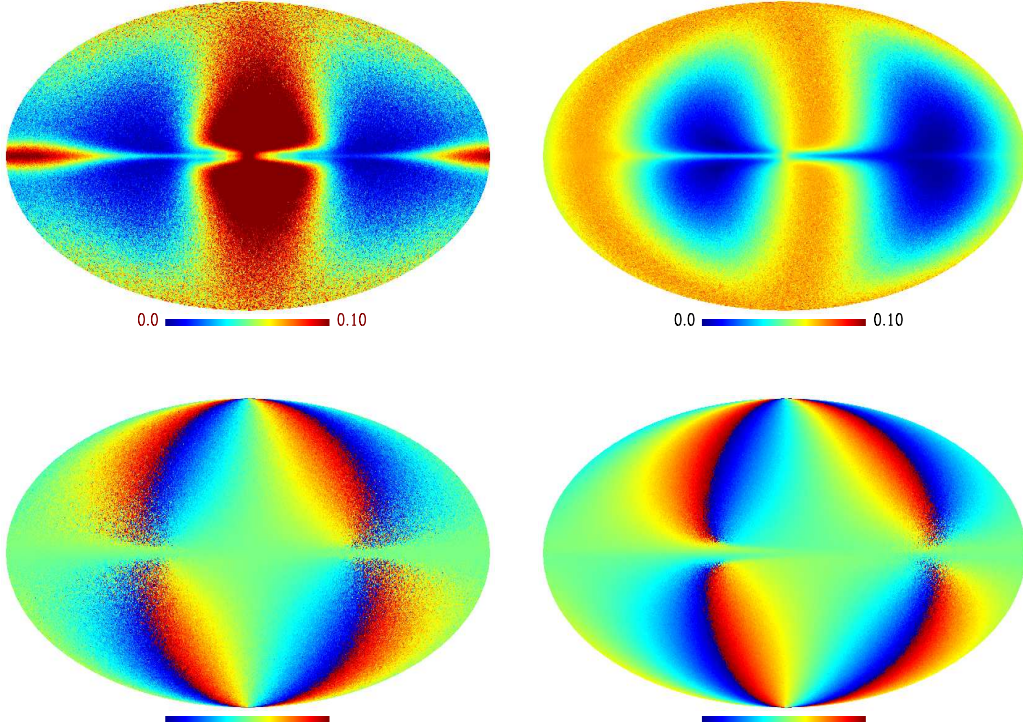


Figure 2. Polarisation fraction (top) and angle (bottom) in Galactic co-ordinates for our model of thermal dust emission at 150 GHz for the BSS (left column) and LSA (right column). The polarisation angle colour bar ranges from $-\pi/2$ to $\pi/2$. Both models include large (ls) and small (ss) scale magnetic field components. The ss turbulent component was added in the one dimensional, line-of-sight approximation and can be seen as an uncorrelated noise addition to the coherent ls component. There are significant differences in the morphology of the polarisation fraction between the BSS and LSA models due to the BSS model including the spiral arm structure.

2.4 Stokes Parameters

We combine the small-scale (ss) and large-scale (ls) magnetic field values according to

$$\begin{aligned} B_r &= B_{r,ss} + B_{r,ls}, \\ B_\theta &= B_{\theta,ss} + B_{\theta,ls}, \\ B_\phi &= B_{\phi,ss} + B_{\phi,ls}, \end{aligned} \quad (4)$$

where r , θ , and ϕ are now Solar-centric spherical polar co-ordinates. The polarisation at each point along the line-of-sight \hat{r} is determined by the perpendicular field components, B_θ and B_ϕ .

The Stokes parameters for this model are projected out from our three-dimensional model using the appropriate line-of-sight integrals,

$$\begin{aligned} I_{\text{model}}(\theta, \phi) &= \epsilon(\nu) \int_0^{r_{\text{max}}} n_d(\mathbf{r}) dr, \\ Q_{\text{model}}(\theta, \phi) &= \epsilon(\nu) \int_0^{r_{\text{max}}} n_d(\mathbf{r}) p_0 [B_\phi(\mathbf{r})^2 - B_\theta(\mathbf{r})^2] dr, \\ U_{\text{model}}(\theta, \phi) &= \epsilon(\nu) \int_0^{r_{\text{max}}} n_d(\mathbf{r}) p_0 [2B_\phi(\mathbf{r})B_\theta(\mathbf{r})] dr, \end{aligned} \quad (5)$$

and the normalisation p_0 is set to reproduce the average polarisation fraction reported by WMAP outside their P06 mask, 3.6% (Kogut et al. 2007). Here, ϵ is the emissivity of the dust as a function of frequency, ν . Note that we conform

to the default convention applied in the HEALPIX¹ package (Górski et al. 2005) regarding the sign of U .

We have chosen the 3.6% average polarisation fraction as a reference value but the templates can be scaled to fit any other preferred value based on more detailed knowledge of the polarisation fraction in smaller patches of the sky. It is also useful to note that since we rescale the Q and U components the *overall* normalisation of the magnetic field model becomes irrelevant. However, the *relative* contributions from the ls and ss components in the field remains as a model parameter.

For the line-of-sight integrals we integrate from zero out to a maximum line-of-sight distance r_{max} of 30,000 pc. The integrals are discretised in steps of 0.1 pc. The direction of the lines-of-sight are chosen to coincide with the centre of all HEALPIX pixels at a given $N_{\text{side}}^{\text{P}}$, where $N_{\text{side}}^{\text{P}}$ is less than or equal to N_{side} of the total intensity template FDS map.

From this model we require maps of the polarisation direction, γ , and degree, P , which are given by

$$\begin{aligned} P(\theta, \phi) &= \frac{(Q_{\text{model}}^2 + U_{\text{model}}^2)^{\frac{1}{2}}}{I_{\text{model}}}, \\ \gamma(\theta, \phi) &= \frac{1}{2} \arctan \left(\frac{U_{\text{model}}}{Q_{\text{model}}} \right). \end{aligned} \quad (6)$$

¹ See <http://healpix.jpl.nasa.gov>

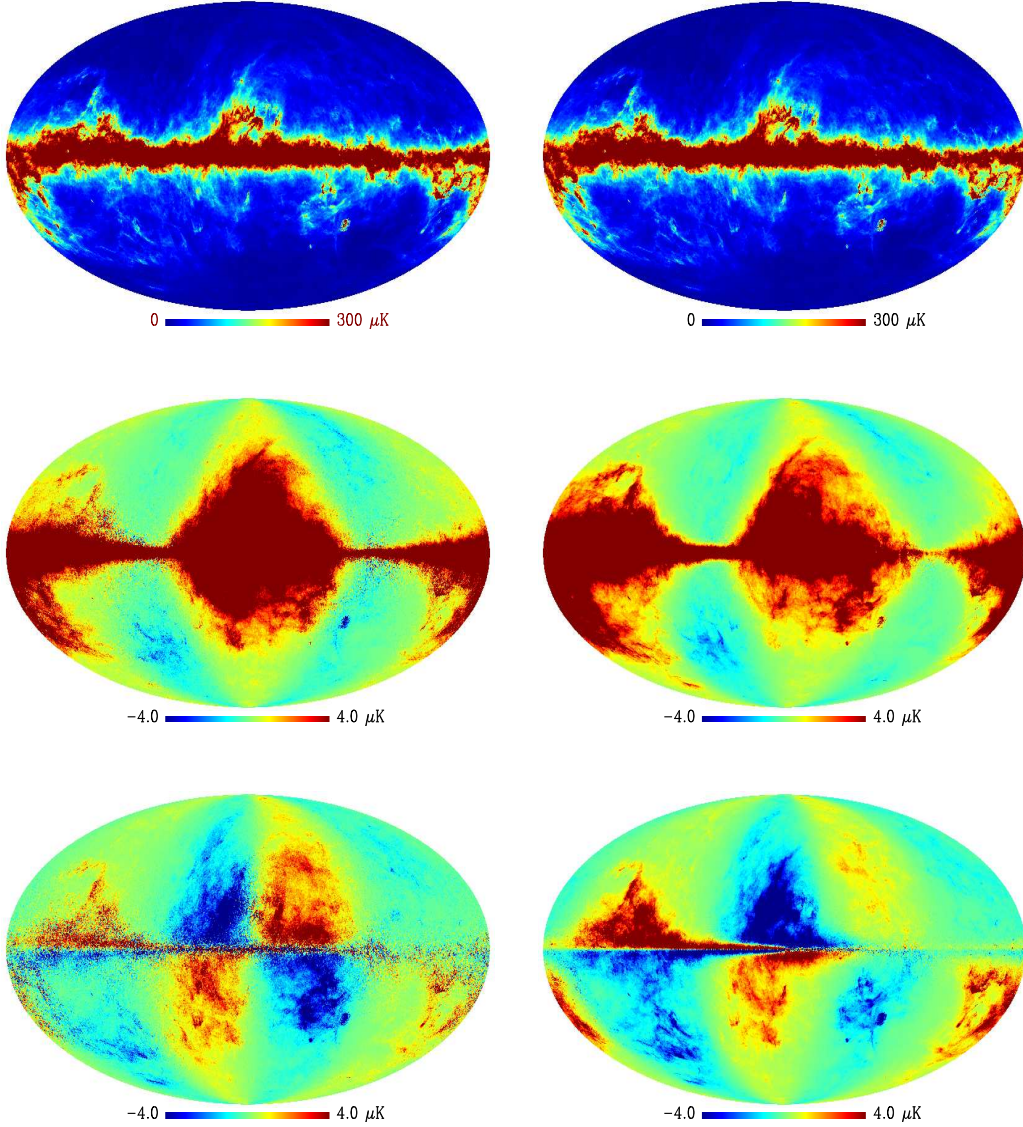


Figure 3. Stokes parameter maps (from top to bottom I , Q and U) in Galactic co-ordinates for our model of thermal dust emission at 150 GHz for the BSS (left column) and LSA (right column).

Figure 2 shows maps of P and γ obtained from a line-of-sight integration at resolution $N_{\text{side}}^{\text{P}} = 128$ for the BSS and LSA magnetic field models including a one dimensional, small-scale turbulent component. The turbulent component is seen here as an uncorrelated noise contribution to the large-scale correlations induced by the large-scale magnetic field model. These maps can be compared to the “geometric suppression” factor shown in the right panel of Figure 8 of Page et al. (2007). There are significant differences between the BSS and LSA field models in the morphology of the polarisation fraction on the sky. The difference is greatest towards the Galactic centre and bulge and the Galactic anti-centre which coincides with a spiral arm. The LSA model does not include any azimuthal dependence and as such does not model any modulation of the magnetic field strength between spiral arms. In addition, the pitch angle of the LSA

model, as fit to the WMAP data, is very low and this leads to a very mild dependence of the field alignment in the radial direction. These differences lead to a significantly simpler polarisation structure in the LSA model than in the BSS case which models the spiral arm structure explicitly.

The final dust model at frequency ν can be written as

$$\begin{aligned} I_{\text{dust}}^{\nu}(\theta, \phi) &= I_{\text{FDS}}^{\nu}(\theta, \phi), \\ Q_{\text{dust}}^{\nu}(\theta, \phi) &= I_{\text{FDS}}^{\nu}(\theta, \phi) P(\theta, \phi) \cos(2\gamma(\theta, \phi)), \\ U_{\text{dust}}^{\nu}(\theta, \phi) &= I_{\text{FDS}}^{\nu}(\theta, \phi) P(\theta, \phi) \sin(2\gamma(\theta, \phi)), \end{aligned} \quad (7)$$

where I_{FDS}^{ν} is the total intensity FDS prediction.

Our final product is a template foreground map with small-scale structure modeled by the FDS predictions in the total intensity but with polarisation fraction and angle determined *internally* by our magnetic field model and line-of-sight integrals. An alternative approach taken by Page et al.

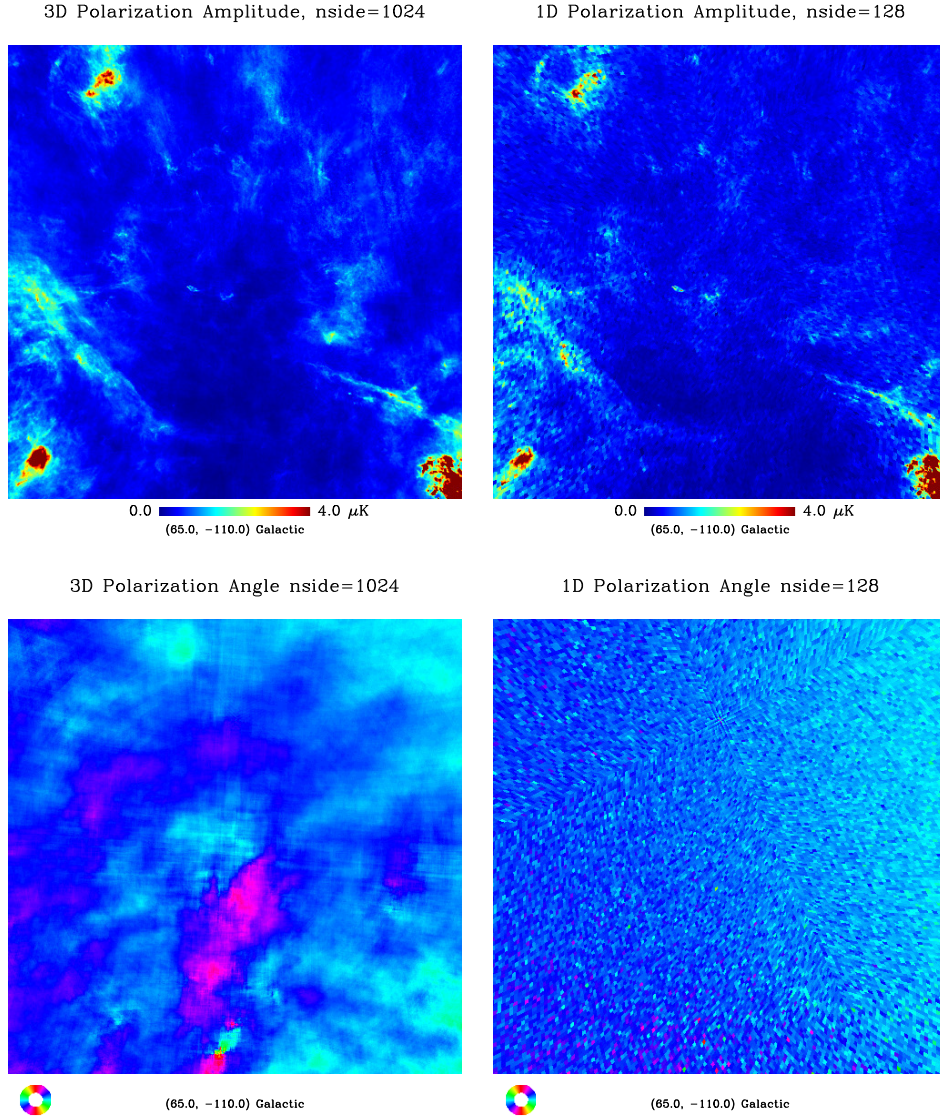


Figure 4. Gnomonic projection of the polarisation amplitude and angle in a 75×75 degree patch in the southern Galactic hemisphere. The left column shows the amplitude and angle from a line-of-sight integration including a full three dimensional realisation of the small-scale turbulent magnetic field model. $N_{\text{side}}^{\text{P}} = 1024$ was used to calculate the “3D” maps but only for lines-of-sight corresponding to pixels inside the patch. The right column shows the same area from the full-sky templates with $N_{\text{side}}^{\text{P}} = 128$. The full-sky maps used a one dimensional realisation of the turbulent component along the line-of-sight to speed up the computation. The absence of correlated small-scale structure and lower angular resolution of polarisation information in the “1D” case is clearly seen when comparing maps.

(2007) is to replace γ with a map $\gamma_{\text{dust}} = \gamma_{\star} + \pi/2$ where γ_{\star} is a smoothed map of observed starlight polarisation directions. This approach, however, is limited by the resolution of the starlight data with only 1578 observations scattered around the sky. It also requires a large smoothing kernel of approximately 10 degrees in size and limits the application of any template derived in this way to very large scales on the sky, corresponding to angular multipoles $\ell \lesssim 15$, and Galactic latitudes $|b| > 10^\circ$.

3 SCALES

It is important to consider the range in angular scales our model is valid for. All our maps are pixelised at $N_{\text{side}} = 1024$, this ensures that the small-scale structure in the FDS prediction is oversampled since the IRAS resolution translates into a limit in angular multipoles of roughly $\ell_{\text{FDS}} \sim 1700$ and the HEALPIX pixel smoothing scale is $\ell_{\text{pix}} \sim 4 N_{\text{side}}$. The overall, effective resolution of our templates is therefore limited by the angular resolution of our line-of-sight coverage which is set by the HEALPIX resolution $N_{\text{side}}^{\text{P}}$.

For the full-sky maps presented here and made available publicly we have chosen $N_{\text{side}}^{\text{P}} = 128$ which corresponds to a limit of roughly $\ell \sim 500$ in multipole space. We also show in our example maps a small patch prediction with $N_{\text{side}}^{\text{P}} =$

1024 (see Section 4) which again oversamples the resolution given by the FDS templates.

It is also important to consider *physically* relevant scales that enable the interpretation of the structure in our templates. The most important of these is the injection scale for the turbulent, small-scale component of the magnetic field. We have set this to 100 pc. To obtain a rough estimate of the angular scales at which this physical scale becomes important we can use a “dust weighted” distance measure $\langle r \rangle = \int r n_d(\mathbf{r}) dr / \int n_d(\mathbf{r}) dr \sim 7000$ pc for a mid-Galactic latitude line-of-sight. This can be used to place the angular multipole scale of injection at $\ell_{\text{inj}} \sim 220$ or roughly 1 degree. Beyond these scales the stochastic, turbulent component begins to dominate the structure in the polarisation and the model is only a statistical description of the real sky on these scales. An exhaustive exploration of foreground effects on scales below a degree would therefore require a Monte Carlo approach.

4 MAPS

We show a selection of template, full-sky maps at 150 GHz in Figure 3. I , Q , and U Stokes parameters are shown for both BSS and LSA derived templates (other frequencies are available on the on-line repository). The maps are of thermodynamic CMB temperature in μK units and are shown in Galactic co-ordinates².

As detailed above, the Q and U components have been normalised such that the average polarisation fraction outside the area defined by the WMAP *P06* mask is 3.6%. The resolution of the HEALPIX maps is $N_{\text{side}} = 1024$ but the polarisation information is based on a line-of-sight integral at an angular resolution of $N_{\text{side}}^{\text{P}} = 128$.

The maps have been obtained by the line-of-sight integration of a magnetic field model that includes a small-scale turbulent realisation only along the line-of-sight direction, ie. our “one dimensional” approximation. Whilst computationally intensive, “3D”, full-sky maps that include a full three dimensional realisation of the turbulent component can be obtained, if required, with computation times of the order of 10 days. However we show results for a smaller 75×75 degree patch in the southern Galactic hemisphere in Figure 4. These maps were obtained using a full three dimensional realisation at an angular line-of-sight resolution of $N_{\text{side}}^{\text{P}} = 1024$ and are compared with the same patch in the full-sky “1D” maps. The difference between the two is most clearly seen in comparing the polarisation angle which is uncorrelated with the FDS intensity template. The full three dimensional case contains correlated structure on smaller scales due to the coloured power spectrum of the realisation. In contrast the one dimensional case is uncorrelated on small scales whilst preserving the large-scale correlations induced by the fixed, large-scale magnetic field model. Tailored, high-resolution, “3D” realisations of small patches such as those shown in Figure 4 are most useful for sub-orbital experiments that can only observe a limited fraction of the sky.

² Care must be taken in rotating Stokes parameters into other co-ordinate systems such as ecliptic and we have provided rotated maps on the on-line repository since most applications will simulate observations in this frame.

5 CONCLUSIONS

We have described a model of the polarised foreground that we expect to observe due to emission from dust within our Galaxy. The model uses a three-dimensional model of the Galactic magnetic field and dust field and integrates along the line-of-sight to each HEALPIX pixel to obtain a polarisation amplitude and angle. This information is combined with total intensity, FDS derived template maps at different frequencies to obtain a complete, polarisation template of foreground emission by interstellar dust.

We have concentrated on two popular models for the structure of the large-scale structure of the Galactic magnetic field, namely, the BSS and LSA models. The parameters for the BSS model have been calibrated directly from measurements of the strength of the Galactic magnetic field. In the LSA case we have employed the parameters obtained by Page et al. (2007) in fitting to the WMAP observations. We calculate the polarisation alignment *internally* to our model in both cases since there is not sufficient external information on polarisation angles at resolutions relevant in this work. Some differences exist between the BSS and LSA derived templates but these are mostly at low Galactic latitudes away from the Galactic centre and as such experiments targeting small areas at high Galactic latitudes will not be sensitive to the differences. The differences do indicate however that a more accurate model of the Galactic magnetic field is required to produce realistic polarisation templates for low Galactic latitudes. In the future, the PLANCK mission will provide an important test of Galactic magnetic field models through detailed characterisation of galactic foregrounds.

We have developed a one dimensional approximation of the stochastic, turbulent, small-scale component of the field for obtaining full-sky templates. A full three dimensional realisation of the turbulent component can be used to obtain higher resolution templates for smaller patches of the sky.

In future work we will be extending the model to include synchrotron emission to form a complete picture of foreground emission relevant for polarisation experiments. Other developments will be required to increase the fidelity of the templates on small scales. These include the addition of a stochastic, small-scale density field to model small-scale structure in the density. In full “3D” calculations this will require the generation of an additional three dimensional, turbulence realisation which is correlated to the small-scale magnetic field. In addition, it would be useful to develop a simple model for the correlation of both realisations with the small-scale structure in the FDS derived total intensity templates.

There is significant freedom in the parameters defining the small-scale structure in the templates. Experiments targeting small angular scales over small patches of the sky will be most sensitive to variations in the parameters and also to the stochasticity of the structure in the templates. Further Monte Carlo explorations of the variation in the maps is therefore warranted to quantify the impact of foregrounds on future sub-orbital experiments. As part of future work we will generate large ensembles of random realisations of the templates on small patches of the sky for the purpose of Monte Carlo studies.

The maps obtained from this model are available for use and can be downloaded from an on-line repository³.

ACKNOWLEDGMENTS

We acknowledge useful discussions with the SPIDER team and in particular with Cynthia Chiang and Aurélien Fraisse. Daniel O’Dea and Carlo Contaldi acknowledge support from STFC under the standard grant scheme (PP/E002129). Caroline Clark is supported by an STFC studentship. Carolyn MacTavish is supported by a Kavli Institute Fellowship at the University of Cambridge. Calculations were carried out on a facility provided by the Imperial College High Performance Computing Service⁴.

REFERENCES

- Armstrong J. W., Rickett B. J., Spangler S. R., 1995, *ApJ*, 443, 209
- Barkats D. et al., 2005, *ApJL*, 619, L127
- Bennett C. L. et al., 2003, *ApJS*, 148, 97
- Benoît A. et al., 2004, *A&A*, 424, 571
- Bierman E. M. et al., 2011, *ArXiv e-prints*
- Bischoff C. et al., 2008, *ApJ*, 684, 771
- Brandt W. N., Lawrence C. R., Readhead A. C. S., Pakianathan J. N., Fiola T. M., 1994, *ApJ*, 424, 1
- Brown M. L. et al., 2009, *ApJ*, 705, 978
- Charlassier R., the BRAIN Collaboration, 2008, *ArXiv preprint*
- Chiang H. C. et al., 2010, *ApJ*, 711, 1123
- Cho J., Lazarian A., 2008, *ArXiv e-prints*
- Culverhouse T. et al., 2010, *ApJ*, 722, 1057
- Dickinson C., Peel M. W., Vidal M., 2011, *ArXiv e-prints*
- Drimmel R., Spergel D. N., 2001, *ApJ*, 556, 181
- Eriksen H. K. et al., 2006, *ApJ*, 641, 665
- Essinger-Hileman T. et al., 2010, *ArXiv e-prints*
- Fauvet, L. et al., 2011, *A&A*, 526, A145
- Filippini J. P. et al., 2010, *Proc. SPIE*, 7741, 77411N
- Finkbeiner D. P., Davis M., Schlegel D. J., 1999, *ApJ*, 524, 867
- Fosalba P., Lazarian A., Prunet S., Tauber J. A., 2002, *ApJ*, 564, 762
- Gold B. et al., 2009, *ApJS*, 180, 265
- Górski K. M., Hivon E., Banday A. J., Wandelt B. D., Hansen F. K., Reinecke M., Bartelmann M., 2005, *ApJ*, 622, 759
- Han J. L., Manchester R. N., Lyne A. G., Qiao G. J., van Straten W., 2006, *ApJ*, 642, 868
- Han J. L., Qiao G. J., 1994, *A&A*, 288, 759
- Haverkorn M., Gaensler B. M., McClure-Griffiths N. M., Dickey J. M., Green A. J., 2006, *ApJS*, 167, 230
- Heiles C., 1996, *ApJ*, 462, 316
- Hoang T., Lazarian A., 2008, *MNRAS*, 388, 117
- Jaffe T. R., Leahy J. P., Banday A. J., Leach S. M., Lowe S. R., Wilkinson A., 2010, *MNRAS*, 401, 1013
- Jansson R., Farrar G. R., Waelkens A. H., Enßlin T. A., 2009, *JCAP*, 7, 21
- Kamionkowski M., Kosowsky A., Stebbins A., 1997, *Phys-RevD*, 55, 7368
- Keating B., Timbie P., Polnarev A., Steinberger J., 1998, *ApJ*, 495, 580
- Kogut A. et al., 2007, *ApJ*, 665, 355
- Kovac J. M., Leitch E. M., Pryke C., Carlstrom J. E., Halverson N. W., Holzapfel W. L., 2002, *Nature*, 420, 772
- Lazarian A., Cho J.-Y., 2003, *Polarized Foreground Emission from Dust: Grain Alignment and MHD Turbulence*, Pandalai, S. G., ed., pp. 255–274
- Lazarian A., Hoang T., 2007, *MNRAS*, 378, 910
- Lazarian A., Hoang T., 2009, *ArXiv e-prints*
- Lazarian A., Pogosyan D., 2000, *ApJ*, 537, 720
- Lazear J. et al., 2011, in *American Astronomical Society Meeting Abstracts #218*, pp. #233.01–+
- Leitch E. M., Kovac J. M., Halverson N. W., Carlstrom J. E., Pryke C., Smith M. W. E., 2005, *ApJ*, 624, 10
- López-Caraballo C. H., Rubiño-Martín J. A., Rebolo R., Génova-Santos R., 2011, *ApJ*, 729, 25
- Macellari N., Pierpaoli E., Dickinson C., Vaillancourt J., 2011, *ArXiv e-prints*
- McMahon J. J. et al., 2009, in *American Institute of Physics Conference Series*, Vol. 1185, American Institute of Physics Conference Series, B. Young, B. Cabrera, & A. Miller, ed., pp. 511–514
- Men H., Ferrière K., Han J. L., 2008, *A&A*, 486, 819
- Minter A. H., Spangler S. R., 1996, *ApJ*, 458, 194
- Miville-Deschênes M., Ysard N., Lavabre A., Ponthieu N., Macías-Pérez J. F., Aumont J., Bernard J. P., 2008, *A&A*, 490, 1093
- Montroy T. E., Ade P. A. R., Bock J. J., Bond J. R., Borrill J., Boscaleri A., Cabella P., Contaldi C. R., 2006, *ApJ*, 647, 813
- Niemack M. D. et al., 2010, in *Society of Photo-Optical Instrumentation Engineers (SPIE) Conference Series*, Vol. 7741, Society of Photo-Optical Instrumentation Engineers (SPIE) Conference Series
- O’Dea D. T., 2009, *PhD thesis*, University of Cambridge, UK
- O’Dea D. T. et al., 2011, *ArXiv e-prints*
- Page L. et al., 2007, *ApJS*, 170, 335
- Piacentini F. et al., 2006, *ApJ*, 647, 833
- Ponthieu N. et al., 2005, *A&A*, 444, 327
- QUIET Collaboration, 2010, *ArXiv e-prints*
- Readhead A. C. S., Myers S. T., Pearson T. J., Sievers J. L., Mason B. S., Contaldi C. R., Bond J. R., Bustos R., 2004, *Science*, 306, 836
- Reichborn-Kjennerud B. et al., 2010, in *Society of Photo-Optical Instrumentation Engineers (SPIE) Conference Series*, Vol. 7741, Society of Photo-Optical Instrumentation Engineers (SPIE) Conference Series
- Sievers J. L. et al., 2007, *ApJ*, 660, 976
- Stompor R., Leach S., Stivoli F., Baccigalupi C., 2009, *MNRAS*, 392, 216
- Sun X. H., Reich W., Waelkens A., Enßlin T. A., 2008, *A&A*, 477, 573
- The Planck Collaboration, 2006, *ArXiv e-prints*
- The Polarbear Collaboration et al., 2010, *ArXiv e-prints*
- Veneziani M. et al., 2010, *ApJ*, 713, 959
- Wu J. H. P. et al., 2007, *ApJ*, 665, 55

³ <http://www.imperial.ac.uk/people/c.contaldi/fgpol>

⁴ <http://www.imperial.ac.uk/ict/services/teachingandresearchservices/highperformancecomputing>